Parametric Study of Peripheral Nozzle Configurations for Supersonic Retropropulsion

Noël M. Bakhtian*
Stanford University, Stanford, California 94305
and
Michael J. Aftosmis†
NASA Ames Research Center, Moffett Field, California 94035

With sample-return and manned missions on the horizon for Mars exploration, the ability to decelerate high-mass systems to the planet's surface has become a research priority. This paper explores the use of supersonic retropropulsion, the application of jets facing into the freestream, as a means of achieving drag augmentation. Numerical studies of retropropulsion flows were conducted using a Cartesian Euler solver with adjoint-driven mesh refinement. After first validating this simulation tool with existing experimental data, a series of three broad parametric studies comprising 181 total runs was conducted using tri- and quad-nozzle capsule configurations. These studies chronicle the effects of nozzle location, orientation, and jet strength over Mach numbers from two to eight and angles of attack ranging from −5 to 10°. Although many simulations in these studies actually produced negative drag augmentation, some simulations displayed local overpressures 60% higher than that possible behind a normal shock and produced drag augmentation on the order of 20%. Examination of these cases leads to the development of an aerodynamic model for significant drag augmentation in which the retrojets are viewed as oblique shock generators and flow approaching the capsule face is decelerated and compressed by multiple oblique shocks. By avoiding the massive stagnation pressure losses associated with the bow shock in typical entry systems, this approach achieves significant overpressure on the capsule face and strong drag amplification. With a fundamental physical mechanism for drag augmentation identified, follow-on studies are planned to exploit this feature and to understand its impact on potential entry trajectories and delivered mass limits for future Mars missions.

Nomenclature

A	=	area, m^2
C_A	=	coefficient of axial force
$C_{A,\text{aeroshell}}$	=	C_A on the aeroshell (not including engine thrust)
$C_{A,\text{forebody}}$	=	C_A on the capsule face
$C_{A,\text{total}}$	=	coefficient of total axial force [see Eq. (8)]
C_D	=	coefficient of drag
C_L	=	coefficient of lift
C_P	=	coefficient of pressure
$C_{P_{oNS}}$	=	stagnation C_P behind normal shock at M_∞
C_T	=	thrust coefficient [see Eq. (9)]
D	=	drag force, N
D_{aug}	=	drag augmentation [see Eq. (10)]
D_{ref}	=	baseline (reference) drag value
d	=	diameter, m
F	=	force, N
$\mathcal{J}$	=	exact functional value
M	=	Mach number
$\mathcal{P}$	=	parametric space
P	=	pressure, Pa
P_{o1}	=	stagnation pressure in front of shock, Pa
P_{o2}	=	stagnation pressure behind shock, Pa
P_{oBS}	=	stagnation pressure behind bow shock, Pa
P_{oNS}	=	stagnation pressure behind normal shock, Pa
P_{oOS}	=	stagnation pressure behind oblique shock, Pa
q	=	dynamic pressure, Pa
r	=	radius, m
r_{nc}	=	nozzle circle radius (see Fig. 12)
T	=	thrust in axial direction, N
u, v, w	=	velocity components, m/s
$()_b$	=	capsule base
$()_e$	=	nozzle exit
$()_o$	=	stagnation
$()^*$	=	nozzle throat
$()'$	=	nondimensional
$()_\infty$	=	freestream
α	=	angle of attack, deg
β	=	ballistic coefficient [see Eq. (1)], kg/m^2
γ	=	ratio of specific heats
θ	=	angular coordinate (see Fig. 10), deg
ρ	=	density, kg/m^3
ϕ	=	nozzle tilt angle (see Fig. 12), deg

I. Introduction

MARS entry poses a challenge due to the planet's thin atmosphere. With only about 1% of Earth's atmospheric density, Mars entry vehicles decelerate at much lower altitudes and have trouble attaining sufficiently low terminal descent velocities without the aid of entry, descent, and landing (EDL) systems such as supersonically-deploying parachutes [1]. To date, the United States has successfully landed six systems on the surface of Mars, starting with the Viking I and II missions which landed in 1976. The EDL system developed for these missions was based on a 70 deg sphere cone aeroshell and a supersonic disk-gap-band (DGB) parachute. Amazingly, all subsequent missions including NASA's 2011 Mars mission, the Mars Science Laboratory (MSL), have used only slight variants of this original EDL system [2].

As mission requirements advance, target mass payload demands are increasing and are challenging the limits of current EDL

*Ph.D. Candidate, Department of Aeronautics and Astronautics, Durand Building, 496 Lomita Mall. Student Member AIAA.
†Aerospace Engineer, NASA Advanced Supercomputing Division. Senior Member AIAA.
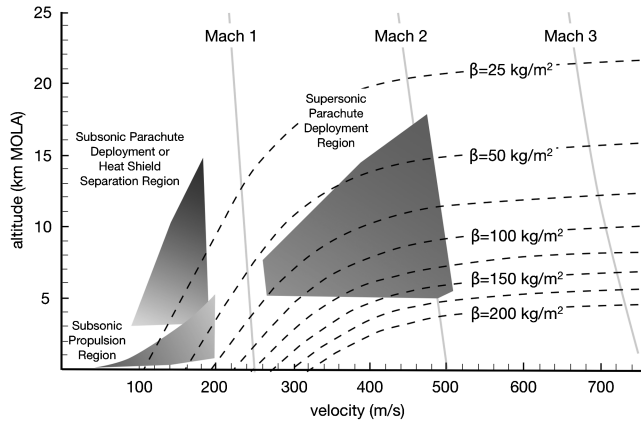
Fig. 1   EDL method deployment regions, adapted from [1].

technology. Each of the six previous Mars missions landed at 0.6t or less, and the upcoming MSL mission has reached the landed payload mass capability (approximately 1 t) of this Viking-based EDL system [2]. Figure 1 shows the limits of the current DGB parachute deployment region and the effect of increasing β, the ballistic coefficient. This value, characterizing the response of an entry vehicle to atmospheric braking, scales directly with mass and is given by

$$\beta = \frac{m}{C_D A} \qquad (1)$$

where m is the system's mass, C_D is the hypersonic drag coefficient, and A is the reference area. As seen in Fig. 1, with increasing payload mass (and thus β), the max-Mach deployment limit of 2.1 for the DGB system is reached at increasingly lower altitudes. For reference, only Mars entry systems with β less than approximately 50 kg/m^2 are able to reach the subsonic propulsion region without supersonic deceleration methods, and all previous missions have ranged from $\beta = 62\text{-}90$ kg/m^2.

Proposed future missions such as the robotic Mars sample-return and the astrobiology field laboratory would result in even higher touchdown masses, and the requirements of human missions to Mars could demand 40–100 t payloads, a two-order of magnitude increase over previous landed mass capability [2]. With these increasingly aggressive payload demands on the horizon, it is evident that the approximate ballistic coefficient limit of the heritage DGB parachute technology, 150 kg/m^2, will be quickly exceeded. The challenges imposed by the large mass requirements of future Mars exploration necessitate the development of additional EDL technologies. Proposed solutions for adequate deceleration include: a) a reduction of the ballistic coefficient through an increase in reference area; b) the development of supersonic parachutes capable of deploying at higher Mach number; c) an increase in vertical lift; or d) the development of a new decelerator such as supersonic retropropulsion (SRP) [1].

This paper examines the development of SRP as a means of deceleration. Historically, retropropulsion has involved the use of thrusters directed into a subsonic freestream flow, the aim of which is to produce a thrust force to supplement the aerodynamic drag, thus providing increased deceleration by increasing the total force on the body. Given the increasing velocities of Mars entry, extension of this deceleration technique to supersonic freestream has been proposed. Recent preliminary SRP development has focused on increasing engine thrust while attempting to maintain the bow shock about the entry body for supplemental drag. The deceleration provided using this strategy is highly dependent on the mass of fuel transported solely for atmospheric entry. In this study, we consider an alternative role, where SRP is used as a mechanism to increase aerodynamic drag by achieving significant surface overpressures rather than merely rely on fuel transport for terminal thrust augmentation.

The bow shock, considered a key decelerative physical mechanism due to the postshock pressure increase, also drastically reduces the postshock stagnation pressure on the body. This means that the maximum recoverable pressure on the capsule face is severely reduced. For example, at $M_\infty = 6$, the stagnation pressure behind a normal shock has decreased to less than 3% of its initial value ($P_{oNS}/P_{o1} = 0.02965$), meaning that the maximum pressure one can recover behind such a shock has dropped by 97%. Recognizing this, the current study seeks to exploit the available reservoir of potential drag by altering the flow physics of the system through the use of retropropulsive jets.

Very little data has been collected on retropropulsive jets in a supersonic freestream [3]. The majority of research in this area of counterflowing, opposing, and forward-facing jets took place as experimental studies in the 1960s and concentrated on a central single-nozzle configuration [4–8]. The aim of many of these studies was to analyze the effectiveness of a retrojet as a means of reducing drag and surface heating. With the same emphasis on drag reduction, numerous numerical studies on central nozzle configurations have been performed as well [9–13]. These studies show that a single opposing central jet acts as an aerospike, significantly reducing the aerodynamic drag which is the opposite effect of that required by SRP for deceleration [14].

In contrast to these studies on drag-reducing central single-nozzle configurations, there is a lack of research on alternate configurations that might prove useful to the SRP community. The most prominent in the literature are experimental multiple-nozzle configuration observations made by Jarvinen and Adams [15,16], Keyes and Hefner [17], and Peterson and McKenzie [18], which suggest that certain multiple-nozzle configurations maintain the drag resulting from the bow shock in addition to providing deceleration from retrothrust, thus giving some additional retroforce. These studies, although increasing the entire axial force with supplemental thrust, show no increase in aerodynamic drag when compared with the baseline (no SRP) case, leading to a total reliance on the mass of fuel transported for this purpose.

This paper provides a series of broad numerical parametric studies to build a preliminary understanding of the physical mechanisms involved in multinozzle (peripheral) SRP flows. Section II describes the flow solver and grid refinement approach used in this study. Section III offers a brief comparison with experimental data and provides an analysis of the tri- and quad-nozzle parametric studies, leading to the development of a flow model for SRP drag augmentation.

II.   Computational Approach

This study was accomplished using the steady-state simulations and adaptive mesh refinement of the Cart3D simulation package. This section briefly describes the Cartesian-based Euler solver and provides an overview of the adjoint-based mesh refinement module. Finally, applicability of the steady-simulation approach to SRP flows is examined through a comparison with a relevant high-resolution, time-accurate simulation.

A.   Numerical Method

Simulations for this investigation are performed using the Cart3D package. This method uses a parallel, multilevel Euler solver on automatically-generated Cartesian meshes with embedded, cut-cell boundaries. Cart3D, developed by Aftosmis et al. [19,20], has recently been extended to include an adjoint-based mesh adaptation method to guide cell refinement and control discretization errors present within complex flow fields [21–23].

Following the creation of a coarse starting mesh upon which the initial flow solve is computed, a cellwise error-estimate is calculated using the method of adjoint-weighted residuals [21,24]. The mesh is refined according to a "worst things first" strategy, and the process repeats until a minimum error or maximum cell count (user-defined) is reached.

The spatial discretization of the Euler equations uses a cell-centered, second-order accurate, upwind finite-volume method with a weak imposition of solid-wall boundary conditions. Steady-state flow solutions are obtained using a five-stage Runge–Kutta scheme

with local time stepping, using the flux-vector splitting approach of van Leer and multigrid convergence acceleration [19,20,25–27]. The solution algorithm for the adjoint equations utilizes the same parallel, multilevel framework as the base Euler solver [21,22].

Widely used for producing aerodynamic databases in support of engineering analysis and design due to its robustness and speed, this inviscid simulation package suits the parametric nature of this study [28–30]. Moreover, this work focuses on simulations with strong and unfamiliar off-body flow features, making it difficult to manually create appropriate meshes a priori. The adjoint-based mesh adaptive approach described here allows automation of the meshing process, and includes information on mesh convergence and discretization error with each simulation.

B. Adjoint-Based Mesh Refinement

As simulation geometries and flows become more complex, the ability to create a suitable mesh a priori presents an increasing challenge. Parametric and optimization studies amplify this problem by requiring hundreds of potentially unique meshes. We address this need through use of an output-based mesh adaptation method. The following discussion outlines the key steps of this method. Further details are provided in References [21–23].

Here, the end goal of the simulation is to provide a reliable approximation of a functional $\mathcal{J}(Q)$, such as lift or drag, that is itself a function of a flow solution $Q = [\rho, \rho u, \rho v, \rho w, \rho E]^T$ satisfying the steady-state, three-dimensional, discretized Euler equations of a perfect gas:

$$\mathbf{R}\left(\mathbf{Q}_H\right) = 0 \qquad (2)$$

Using $J()$ to represent the discrete operator used to evaluate the functional, $J(\mathbf{Q}_H)$ now denotes the approximation of the functional computed on an affordable (coarse) Cartesian mesh with characteristic cell size H, where $\mathbf{Q} = [\bar{Q}_1, \bar{Q}_2, \ldots, \bar{Q}_N]^T$ is the discrete solution vector of the cell-averaged values for all N cells of the mesh.

Figure 2 shows convergence of a model aerodynamic functional with mesh refinement, where E is the total error in this output due to discretization error in the numerical solution. This error is defined as the difference between the exact functional value and the value obtained when evaluating this functional using the discrete solution on the current mesh, $E = |\mathcal{J}(Q) - J(\mathbf{Q}_H)|$. Rather than attempt to compute E directly, we use the approach of Venditti and Darmofal [24] and consider the simpler problem of estimating how the discrete functional evaluation $J(\mathbf{Q}_H)$ would change if solved on a finer mesh, h. The relative error, sketched in Fig. 2, is defined as the difference between the functional evaluations on the current mesh H and the finer, embedded mesh h:

$$e = |J(\mathbf{Q}_h) - J(\mathbf{Q}_H)| \qquad (3)$$

For a second-order method on a sufficiently smooth solution in the asymptotic range, knowing the relative error gives total error in the output as

$$E = e + \frac{1}{4}e + \frac{1}{4^2}e + \cdots = \frac{4}{3}e \qquad (4)$$

Knowledge of the relative error e, however, hinges on the ability to evaluate the functional using the fine mesh solution, $J(\mathbf{Q}_h)$. Without solving on this finer mesh, an estimate of the functional on the embedded mesh can be found using Taylor series expansions of the functional and residual equations about the coarse mesh solution, given by

$$J(\mathbf{Q}_h) \approx J(\mathbf{Q}_h^H) - \underbrace{(\psi_h^H)^T \mathbf{R}(\mathbf{Q}_h^H)}_{\text{Adjoint correction}} - \underbrace{(\psi_h - \psi_h^H)^T \mathbf{R}(\mathbf{Q}_h^H)}_{\text{Remaining error}} \qquad (5)$$

where $\mathbf{R}()$ is the spatial operator of the Euler solver, ψ is the discrete adjoint solution, and the notation $()_h^H$ indicates prolongation from the coarse to fine mesh [24]. The adjoint variables satisfy the following linear system of equations:
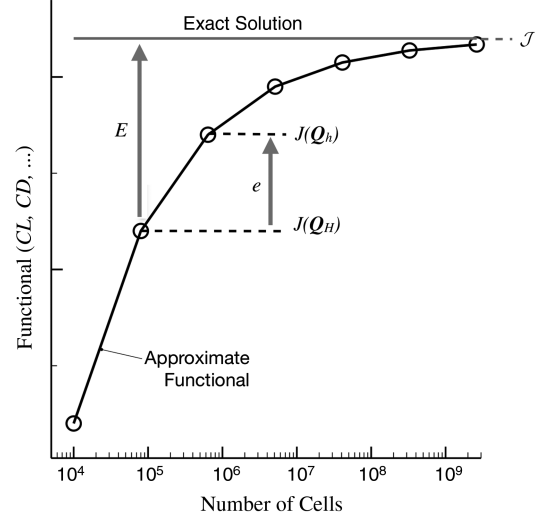

Fig. 2 Convergence of functional J with mesh refinement.

$$\left[\frac{\partial \mathbf{R}(\mathbf{Q}_H)}{\partial \mathbf{Q}_H}\right]^T \psi_H = \frac{\partial J(\mathbf{Q}_H)^T}{\partial \mathbf{Q}_H} \qquad (6)$$

Details on the adjoint solver can be found in [22] and [21,31] contain verification and validation studies on this error-estimation method.

In Eq. (5), the adjoint variables provide two correction terms, one which improves the accuracy of the functional on the coarse mesh, and one serving as a remaining error term which is used to form an estimate of each cell's contribution to the error in the objective function. Convergence of the calculated functional towards its true value occurs as this remaining error term decreases, making the cellwise error-estimate the focus of the adaptation strategy. This term depends on the solution of the adjoint equation on the embedded mesh, ψ_h, but this can be approximated with an interpolated adjoint solution from the coarse mesh [32]. Note that the remaining error is formed through an inner product involving both the flow residual of the prolonged discrete solution (essentially an estimate of local truncation error) and the adjoint interpolation errors (serving as a weighting term). Both of these terms need to be large for cell refinement to improve the functional output, $J(\mathbf{Q})$.

In a typical case using adjoint-based mesh refinement, the corrected functional will lead the computed functional $J(\mathbf{Q}_H)$ towards the true functional value $\mathcal{J}(\mathbf{Q})$ as the number of cells increases. Each of these cycles should see the remaining error value drop as the mesh is refined and $J(\mathbf{Q}_H)$ converges. Figure 3 shows a generic initial mesh (23,000 cells) and an automatically-adapted final mesh (763,000 cells) for one of the cases in the parametric study of Sec. III.C. The functional appears to be approaching an asymptotic value by the fifth adaptation cycle despite the complex flow features, as seen in Fig. 4. This is corroborated by the drop in the functional's error-estimate (the cellwise error summed over all cells), seen in the same figure.

As discussed in [31,32], the error-estimate also reveals the refinement level at which this steady modeling approach begins to break down. An increase in the error-estimate in the final adaptation cycle indicates unsteadiness, or noise due to incomplete flow convergence. The next section compares results obtained with the described steady method to those from a time-accurate simulation of relevant SRP physics, supporting the use of steady simulations in this preliminary study.

C. Comparison with Time-Accurate Simulations

Before proceeding with extensive parametric studies, it is prudent to examine the utility of the described steady and inviscid model when applied to flow physics represented in SRP cases. Examples of comparisons between steady Cart3D simulations and bluff-body time-accurate simulations are given in Reference [32]. We also give a brief comparison with SRP time-accurate simulations here, and
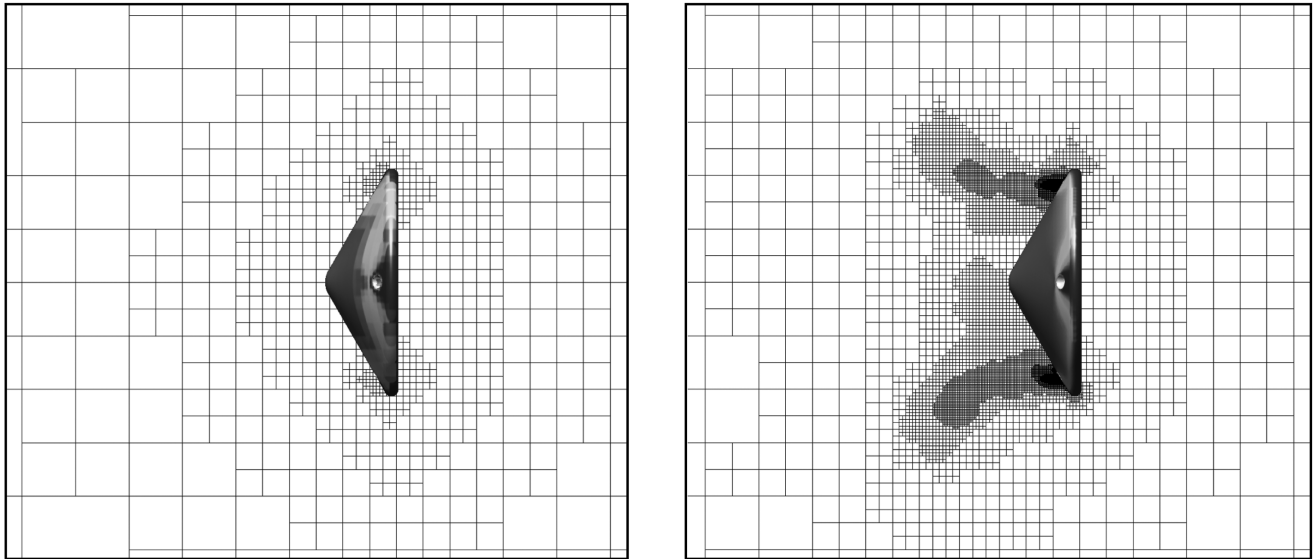
Fig. 3   Initial and final mesh (after five adapt cycles), showing refinement resulting from automatic adjoint-based method.
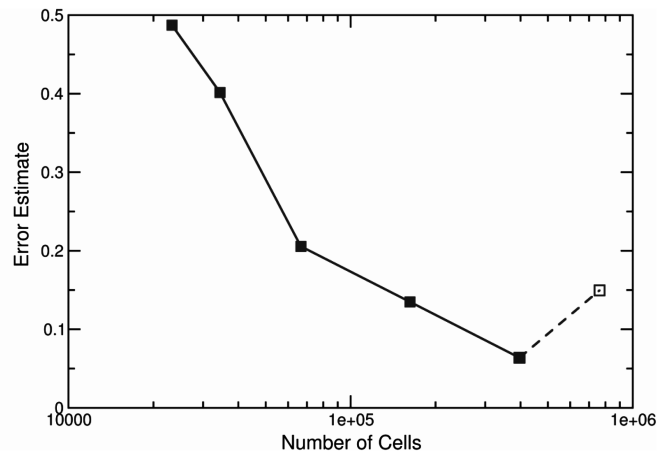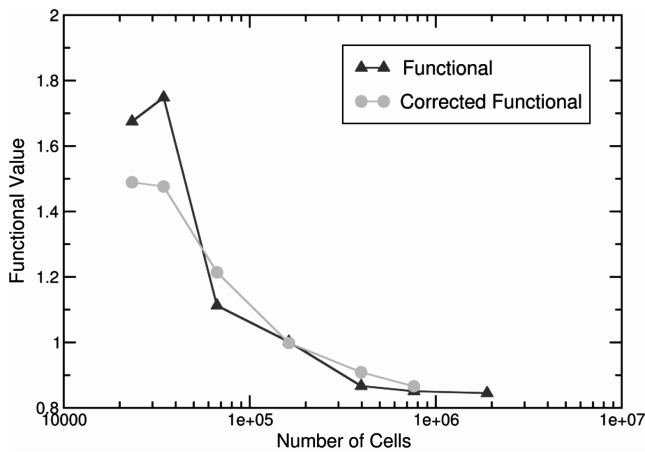

Fig. 4   Convergence of the functional and error-estimate.

provide a comparison against relevant experimental data in Sec. III.A.

Full unsteady simulations were run using a time-accurate version of the Cartesian Euler solver, developed in [33]. This solver uses the same multilevel, parallel framework with time accuracy achieved through a dual-time formulation in which multigrid is used to converge inner pseudotime iterations. Figure 5 contains the 4.5 million cell mesh used for both steady and time-accurate simulations. This mesh was generated by further adaptation of the mesh shown in the previous section.

Figure 6 gives a quantitative comparison between the two simulations by showing the convergence histories of forces on the capsule for the steady simulation as a function of multigrid cycles in the frame on the left and for the unsteady simulation on the right. Computed averages and averaging windows are shown with dotted lines, and force scales are identical in both frames to facilitate comparison. The averaged drag coefficient values for the steady and time-accurate cases are 1.520 and 1.530, respectively. The unsteady simulation required a nondimensional time step of 0.006, based on the freestream speed of sound and the capsule diameter, and was initialized with 200 cycles of multigrid relaxation to produce the time-accurate results in Fig. 6. This simulation required roughly a factor of 50 times more computational effort than the steady results shown adjacent. Given both the close agreement between the time-averaged coefficients and the steady-state results and this wide disparity in computational cost, we used adaptively-refined steady-
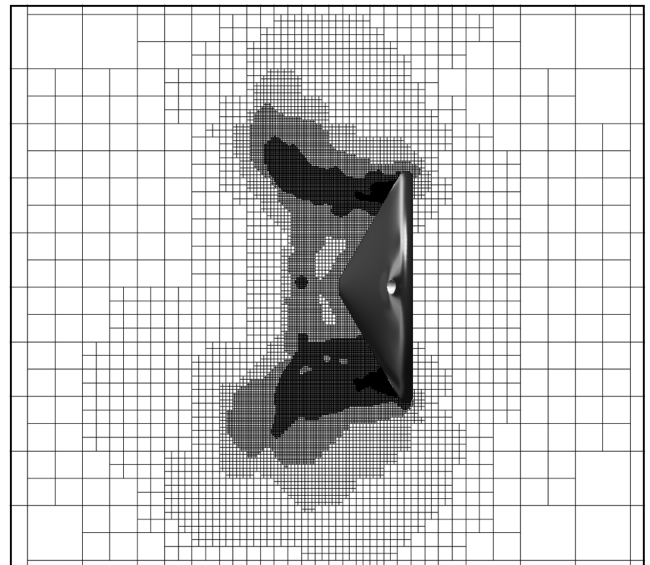

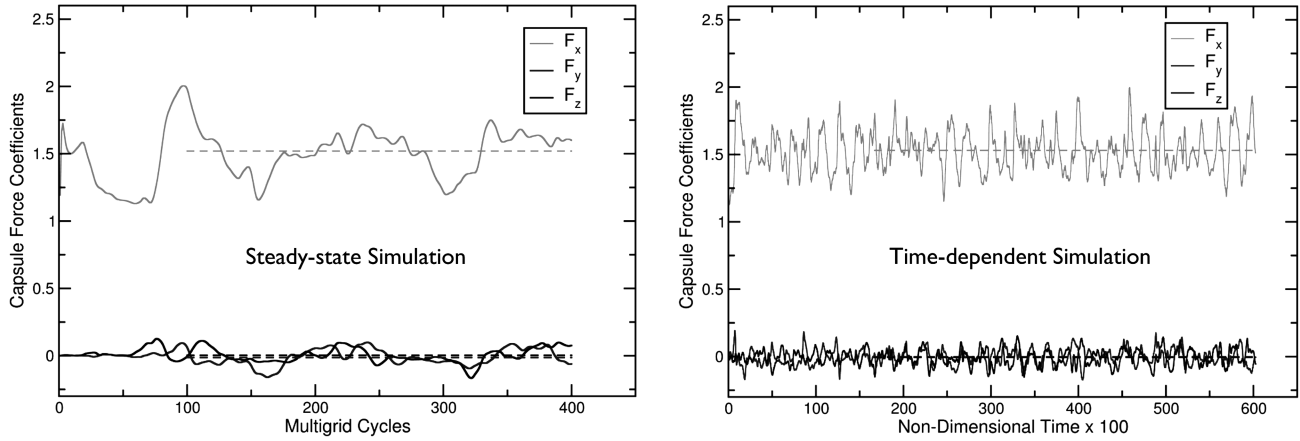Fig. 5   Mesh used for time-accurate simulation comparisons.

Fig. 6   Comparison of force coefficients using steady-state and time-dependent approaches.

state modeling for the simulations in the parametric studies conducted in the present work.

III.   Numerical Simulations and Discussion

The presentation of numerical simulation results opens with a validation study supporting use of the steady, inviscid method described in Sec. II to study problems involving counterflowing jets in a supersonic freestream. A series of parametric studies then highlights the effects of retrojet nozzle placement and jet strength on drag coefficient. These studies increasingly focus on examples which exhibit a substantial capsule face overpressure and establish trends valuable for future design studies. Finally, we introduce a SRP flow model describing a physical mechanism leading to significant drag augmentation, supported by data from the parametric studies.

A.   Comparison with Experimental Data

This section examines the use of the described numerical method for approximating the complexities of SRP flow through a
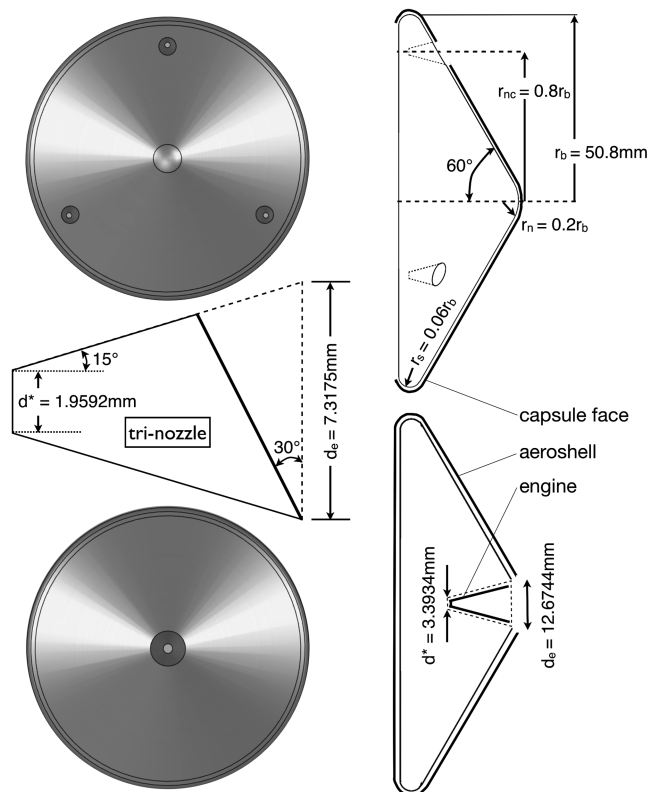

Fig. 7   Geometric details of the tri-nozzle and single-nozzle model geometries.

comparison with experimental SRP data containing the relevant physics. An experimental dataset given in a study by Jarvinen and Adams [15] is used here to compare force and pressure data. Despite several geometrical inconsistencies, test condition omissions, and lack of uncertainty estimates and notes on flow phase and unsteadiness, this study still represents one of the few published surveys on peripheral SRP configurations and is utilized in other recent studies [34,35].

1.   Geometry and Simulation Details

The current simulations use geometries taken from the experimental studies with tri-nozzle and single-nozzle aeroshell configurations, given in [15]. The experiments simulated in this study were conducted on a 60° half angle, conical aeroshell, 101.6 mm in diameter (4 in). Figure 7 and Table 1 give further geometric details of the tri- and single-nozzle configurations, including illustration of the surfaces used in capsule face, aeroshell, and engine force integrations. The three 15°-conical, equally-spaced nozzles of the peripheral tri-nozzle geometry (shown in Fig. 7) are scarfed at 30° by the aeroshell surface. These nozzles are placed such that the center of the throat lies at $0.80 r_b$ from the aeroshell's line of symmetry. The 15°-conical nozzle of the central single-nozzle geometry is placed on the aeroshell's line of symmetry. The final simulation geometries were discretized into 118,000 and 123,000 triangles for the single- and tri-nozzle configurations, respectively.

For this validation study, the baseline tri- and single-nozzle configurations were run at M_∞ and α conditions tested experimentally in [15]. Simulation power boundary conditions, P', ρ', and u', v', and w' were applied at each nozzle throat. We used the incremental mesh refinement method of Sec. II.B, targeting error in the functional chosen as the simple weighted sum of lift and drag coefficients on both the capsule face and the engines:

$$\mathcal{J} = 0.8(C_L + C_D)|_{\text{engines}} + 0.2(C_L + C_D)|_{\text{capsuleface}} \quad (7)$$

Approximately 5 adapt cycles were used in each case, resulting in mesh sizes on the order of 400,000 cells. For this study, jets-off cases were run on geometries with nozzles to be consistent with [15]. In contrast, the parametric studies of Secs. III.B and III.C utilize a clean aeroshell (no nozzles) for baseline cases.

Table 1   Geometry specifications for the two configurations used in the experimental comparison study

Geometry	Tri-nozzle	Single-nozzle
d_b, mm	101.6	101.6
A_b/A_e	192.77651	64.25884
A_e/A^*	13.95	13.95
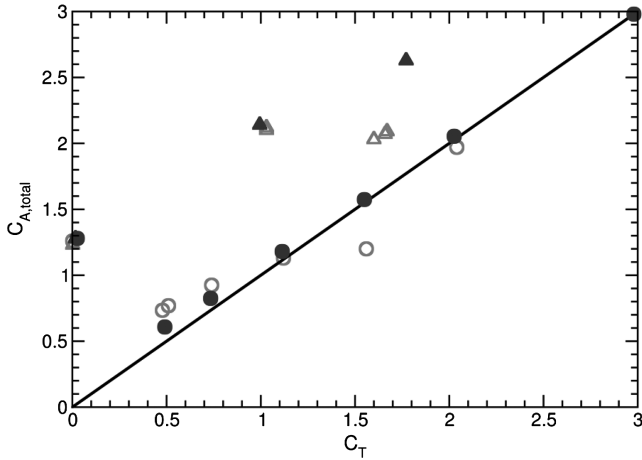
a) Total axial force coefficient
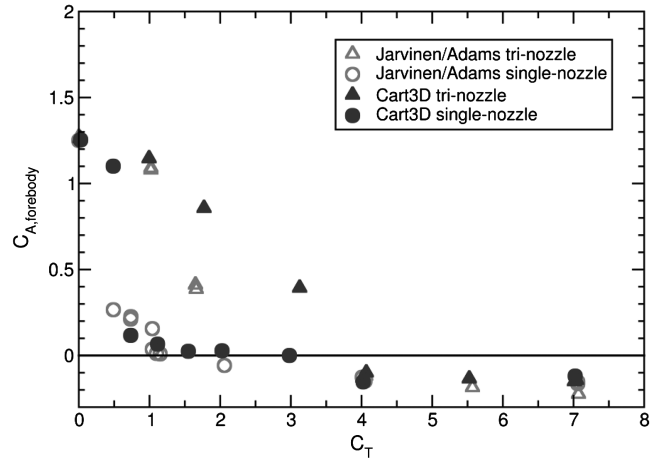
b) Forebody axial force coefficient

Fig. 8 Comparison of experimental and numerical results for both single- and tri-nozzle configurations at $M_\infty = 2$ and $\alpha = 0°$.

2. Comparison of Force and Pressure Data

The experimental work in [15] focused on variations of the total axial force coefficient $C_{A,total}$, which is a sum of the axial thrust coefficient and the axial surface forces acting on the aeroshell:

$$C_{A,total} = C_T + C_{A,aeroshell} \qquad (8)$$

Because of experimental restrictions, accurate pressure measurements could not be taken over the entire capsule base. As a result, the experimental $C_{A,aeroshell}$ was evaluated assuming that freestream static pressure was acting over the entire model base, giving forebody axial force coefficient, $C_{A,forebody}$. To compare with the experimental data, the numerical data was postprocessed with the same technique. Figure 8 shows the numerical and experimental variation in $C_{A,total}$ (here computed as $C_{A,total} = C_{A,forebody} + C_T$) and $C_{A,forebody}$ with thrust coefficient

$$C_T = \frac{T}{q_\infty A_b} \qquad (9)$$

for both the single-nozzle and tri-nozzle geometries at $M_\infty = 2$ and $\alpha = 0°$. It should be noted that delivered thrust coefficient is typically
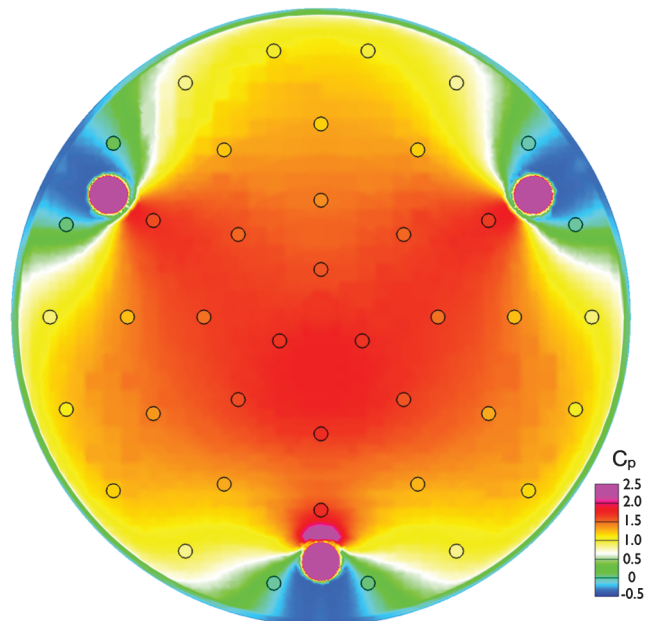
different than requested thrust coefficient due to nozzle scarfing and cosine losses. Experimental values were lifted from Figs. 55 and 56 of [15]. Tri-nozzle results are represented by triangles while circles represent single-nozzle data points. The line in Fig. 8a indicates the values at which $C_{A,total} = C_T$, meaning that the entire axial force on the model is due to the thrust alone and that aerodynamic drag is negligible. Examining the single-nozzle cases in Fig. 8a, total axial force is seen to immediately drop to the thrust level by $C_T = 0.5$. The tri-nozzle cases maintain a higher total axial force at low C_T, but this too drops down, asymptoting to the levels established by the thrust by $C_T = 3$. Numerical data follows these trends closely.

The discrepancy in tri-nozzle data seen at higher C_T levels is better examined in Fig. 8b, which highlights the drag value itself (the force level above the line in Fig. 8a), by plotting $C_{A,forebody}$ as a function of C_T. Here, we can see that the numerical tri-nozzle values do drop to match experimental data at $C_T \geq 4$. This lag in drag reduction with C_T is mirrored, to a lesser extent, in the single-nozzle data as well. Numerical results at $C_T = 0$ are seen to agree with experimental data to within 4%. Of note is the complete lack of aerodynamic drag on the capsule face for the single-nozzle configuration at $C_T > 1$ and the tri-nozzle configuration at $C_T > 3$. This suggests that, at these conditions, a single jet or set of jets (each at $C_T > 1$) actually acts as a drag-resistant aerospike by preventing high pressure from developing on the capsule face.

A similar comparison was also completed both over a range of α values and for $M_\infty = 1.05$ and 1.5. In general, the same trends are seen in both numerical and experimental datasets, and numerical values give a high confidence in the simulation model. The tri-nozzle
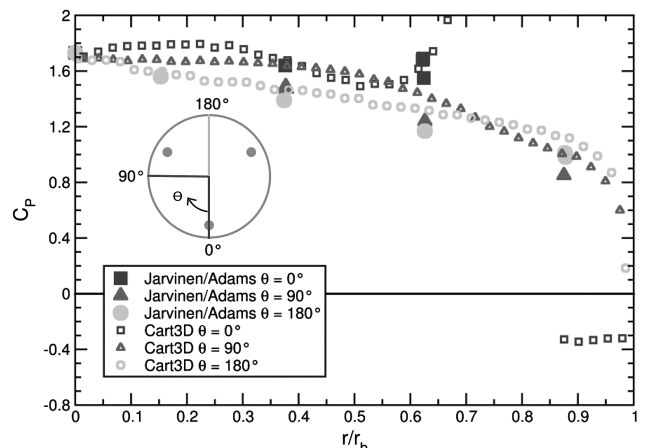

Fig. 9 Experimental and numerical data comparison at $M_\infty = 2$, $\alpha = 0°$, $C_T = 1$.

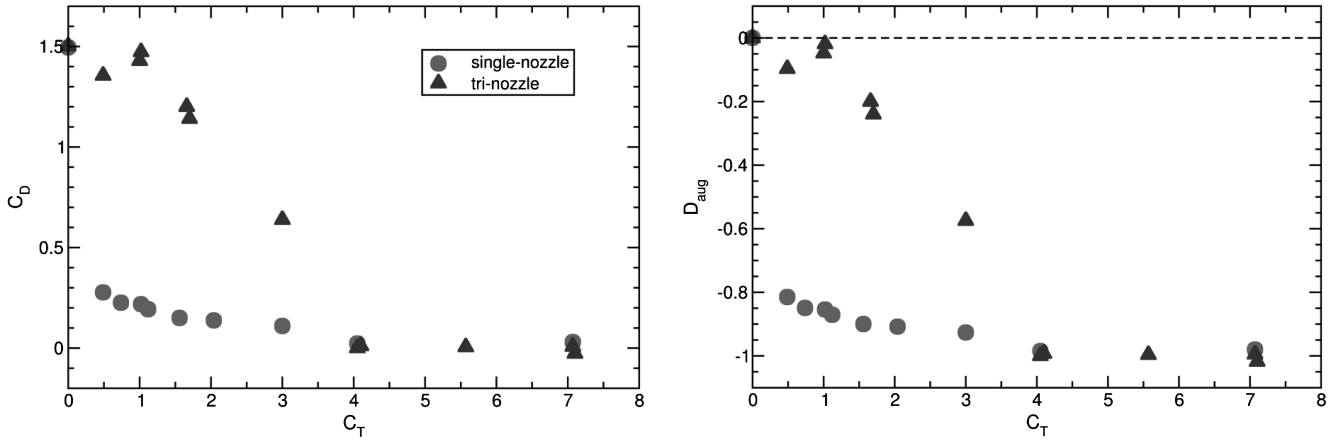Fig. 10 Comparison of experimental and numerical radial pressure profiles for the $M_\infty = 2$, $\alpha = 0°$, $C_T = 1$ case.

Fig. 11 Numerical C_D and D_{aug} data for $M_\infty = 2$ and $\alpha = 0°$.

case at $M_\infty = 2$ and $\alpha = 0°$ with $C_T = 1$ is further highlighted in [15] because it led to one of the highest drag values in the study. Figure 9 shows numerical surface pressure data compared with data taken from experimental pressure taps on the model face (lifted from Fig. 72 of [15]). Experimental pressure coefficients are given in the circles shown at the locations of the respective pressure taps, while the numerical pressure coefficient distribution is shown over the remainder of the capsule face. Surface pressure magnitudes show very good qualitative agreement over the capsule face.

Figure 10 gives a more quantitative view, comparing capsule face surface pressure profiles along radial directions (from nose to periphery) for the same case, with experimental data lifted from Fig. 66 in [15]. The line along $C_p = 0$ represents values at which measured pressure is equal to freestream static pressure. The data are taken along radial lines (constant θ), the positions of which are portrayed in the inset of Fig. 10 ($\theta = \{0°, 90°, 180°\}$). This figure shows the numerical results closely following the experimental trend along each of the radial lines. Radial lines passing between the nozzles ($\theta = 90$ and $180°$) show a maximum pressure at the center of the capsule face with a gradual decrease in the direction of the capsule periphery. The $\theta = 90°$ line, lying $30°$ closer to a nozzle, maintains a higher pressure across more of the capsule face than the $\theta = 180°$ line, but experiences lower pressures in the vicinity of the nozzle. The $\theta = 0°$ line actually cuts through a nozzle, and so hits a maximum pressure on the surface prior to the nozzle. The pressure coefficient behind the nozzle (between the nozzle and the capsule edge) is negative, due to the wake behind the plume. Consistent with Fig. 9, numerical data follows the experimental trends closely, but experiences slightly higher pressures along radial lines between nozzles. The similarities in both values and trends between numerical simulation data and the experimental studies of [15] strongly reinforce our confidence in the simulation ability to capture the relevant SRP flow physics using this inviscid, steady modeling approach.

This analysis, revealing that the beneficial drag force on the body disappears at tri-nozzle C_T levels greater than three, implies that use of SRP in the manner of [15] would be severely limited as a decelerative technique. First, any system requiring more thrust than $C_T = 3$ would need to rely entirely on the thrust for deceleration, since aerodynamic drag is negligible in that range. Second, any system relying on the added benefit of aerodynamic drag in addition to thrust would be limited to operating at C_T levels less than three. Moreover, achieving drag in this manner is limited; it is clear from Fig. 8b that SRP ($C_T > 0$) in the experimental study consistently decreases the actual aerodynamic drag experienced by the body. This can be expressed as a negative drag augmentation, with drag augmentation due to jet interaction (JI) defined as

$$D_{aug} = \frac{D - D_{ref}}{D_{ref}} \quad (10)$$

where the reference drag value here is the drag experienced by a capsule with no SRP ($C_T = 0$) at the same M_∞ and α. With this definition, doubling the baseline drag gives $D_{aug} = 1$, maintaining the baseline drag gives $D_{aug} = 0$, and elimination of all drag results in $D_{aug} = -1$. We see this clearly in Fig. 11, which shows the numerical results of this study plotted as C_D and the corresponding drag augmentation, D_{aug}, with the $C_T = 0$ values for the tri- and single-nozzle configurations used as D_{ref} in Eq. (10). For reference, the dashed line indicates $D_{aug} = 0$. Again it is noted that all of the cases based on the experimental study experienced negative drag augmentation, or a lower drag than achieved by a capsule without SRP. While it is obvious that the deceleration still increases with the thrusting force regardless of the lack of aerodynamic drag, it seems ironic to rely on fuel storage and transport to solve an EDL mass problem without having investigated the potential of drag augmentation. Rather than depend on thrust for deceleration, this study aims to introduce a SRP mechanism by which drag itself is augmented, using a limited amount of thrust. In the absence of further significant multinozzle SRP data, and to explore any possible mechanisms which may lead to significant drag augmentation, several parametric studies were executed and are described in the
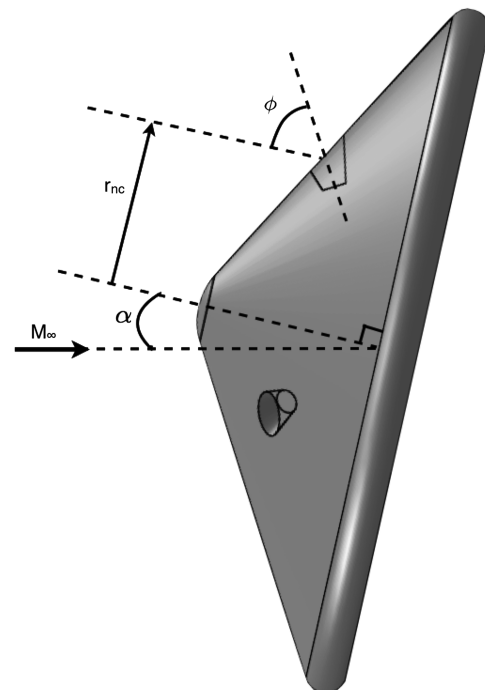

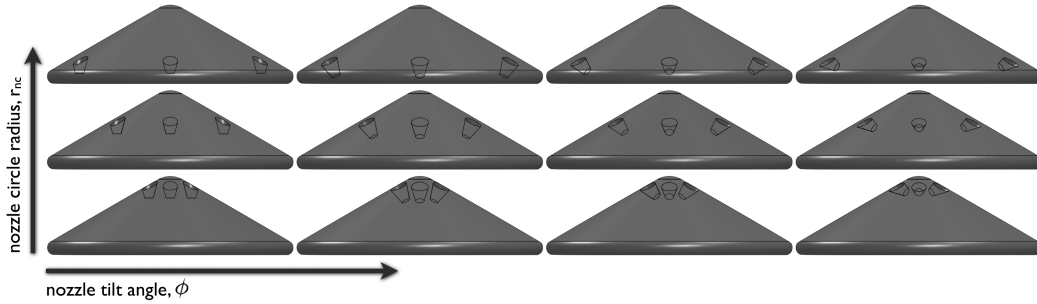Fig. 12 Several variables tested in the parametric study.

Fig. 13   Geometric configurations tested in the initial (tri-nozzle) parametric studies.

next sections, varying jet strength, placement, and orientation over a range of wind-space conditions.

B.   Initial Parametric Study

With the lack of experimental and simulation data from peripheral nozzle configurations over a range of conditions and geometries, a parametric study is performed here to establish a baseline understanding of the physical intricacies of SRP and to determine the potential for drag augmentation. This study uses the Jarvinen and Adams tri-nozzle geometry as a starting point. First, a baseline study is completed, varying nozzle placement, orientation, and jet strength at $M_\infty = 2$ and $\alpha = 0°$. An augmented study follows, extending the analysis to higher freestream Mach numbers.

1.   Geometry and Parameterization

The baseline tri-nozzle geometry used for these parametric studies is based on the configuration used by Jarvinen and Adams ([15]). The aeroshell geometry is the same as that created for the validation study (described in Sec. III.A.1). The three $15°$ conical nozzles, equally-spaced and scarfed by the aeroshell surface, have an $A_e/A* = 4.23$ with $A_b/A_e = 200$.

The parameter space includes variations in nozzle placement and orientation, jet strength, and wind-space conditions. Figure 12 shows the geometric nozzle parameters (r_{nc}, nozzle circle radius as a function of r_b, and ϕ, nozzle tilt) and Fig. 13 shows each of the 12 nozzle configurations. These geometric parameters are varied over a range of freestream Mach numbers, capsule angles of attack, and jet thrust coefficients (defined in Eq. (9)). In total, we examine a five-dimensional parametric space $\mathcal{P} = \mathcal{P}(M_\infty, \alpha, r_{nc}, \phi, C_T)$. Evaluated parametric values are listed in Table 2. In all, 103 simulation cases were run. The baseline tri-nozzle study tests the jet parameters at $M_\infty = 2$ and $\alpha = 0°$. Additional wind-space conditions are then tested in the augmented tri-nozzle study using a subset of the configurations.

2.   Baseline Tri-Nozzle Study

The baseline parametric study consisted of cases varying nozzle placement, orientation, and jet strength over the entire range given in Table 2 at $M_\infty = 2$ and $\alpha = 0°$. In total, 49 cases were run for this study, including the reference jets-off case. This $C_T = 0$ case resulted in a drag coefficient of 1.52 against which all of the retropropulsive cases in this section are compared. The drag augmentation results [Eq. (10) with the $C_T = 0$ case taken as the reference] are given in

Table 2   Range of tested geometric, boundary condition, and wind-space parametric values for the tri-nozzle studies

Variable	Tested values
M_∞	2, 4, 6, 8
α	0°, 10°
r_{nc}	0.2, 0.5, 0.85
ϕ	0°, 30°, 45°, 60°
C_T	0, 0.5, 1, 3, 6

Fig. 14. As described in Sec. III.A.2, drag augmentation gives the relative change in drag as compared with a configuration with no SRP.

Each plot in Fig. 14 compares drag augmentation for capsules with various nozzle positions (r_{nc}) as a function of thrust coefficient, with nozzle tilt (ϕ) varying between each plot. The $r_{nc} = 0.2$ cases, those with nozzles located closest to the center of the capsule, tend to fare the worst, with drag falling towards 0 with increasing thrust coefficient. Negative drag, or control reversal due to JI, is even experienced at $\phi = 30°$ and $C_T = 6$. In this case, the centrally-placed jets actually act as an aerospike and reduce the drag of the baseline system. The $r_{nc} = 0.85$ cases, however, with nozzles located at the periphery of the capsule, maintain the highest drag even at the larger thrust coefficients (seemingly independent of C_T and ϕ) by holding the plume away from the capsule pressure face, especially at nonzero tilt angles, thus allowing unhindered flow from the bow shock to affect the surface pressure. The low surface pressures experienced by cases with centrally-located nozzles are the result of wake flow or the plume flow itself.

Figure 15 aids in visualizing this low-pressure effect by portraying the differences due to plume position for a set of extreme cases, $\mathcal{P}(M_\infty, \alpha, r_{nc}, \phi, C_T) = \mathcal{P}(2, 0°, \{0.20, 0.50, 0.85\}, 60°, 6)$. The top row of images in Fig. 15 show pressure coefficient on the body and Mach contours on a cutting-plane passing through the center of the capsule and intersecting a nozzle, with flow from left to right. The color map has been chosen to aid in flow comprehension, with white representing Mach 1 contours, blue representing subsonic regions, and yellow to red representing supersonic areas. The lower row of images show the corresponding capsule face pressure coefficients. Here, the color map facilitates visualization of overpressure, with white representing $C_{P_{oNS}}$ (the stagnation pressure coefficient behind a normal shock at M_∞), blue representing underpressure, and yellow to red showing areas of overpressure. From this figure, it is clear that nozzles located at the capsule periphery allow higher pressures over the majority of the capsule face, although no areas of overpressure on the capsule face are evident or expected here.

The only cases in which the peripheral jets decreased the drag significantly were those performed at a nozzle tilt of 0° and high C_T. When the heavy plume flow runs head-on into the freestream flow, a huge wake region forms behind the plume, directly affecting the capsule face and obviating any high surface pressures. At higher tilt angles, the capsule face no longer lays in the wake of this interaction region, allowing the surface to maintain its postbow shock surface pressures and thus maintain its baseline drag value.

The major observation in this study is the lack of drag augmentation in a majority of the cases. At best, the peripheral jets manage to maintain the drag obtainable without retropropulsion (just a capsule with bow shock), while a majority of the more centrally-located jet configurations actually resulted in a severe decrease in drag as compared with this reference. Three cases, $\mathcal{P}(M_\infty, \alpha, r_{nc}, \phi, C_T) = \mathcal{P}(2, 0°, 0.85, 60°, \{3, 6\})$ and $\mathcal{P}(2, 0°, 0.85, 45°, 3)$, marginally augmented the drag, giving maximum D_{aug} values of 0.030 (a 3% drag increase). By simply straightening the bow shock (Fig. 16), the freestream flow experiences a lengthened section of normal shock in front of the capsule face leading to slightly increased pressures on the face. With the plumes caught between the bow shock and the body, this is the only mechanism by which the capsule face
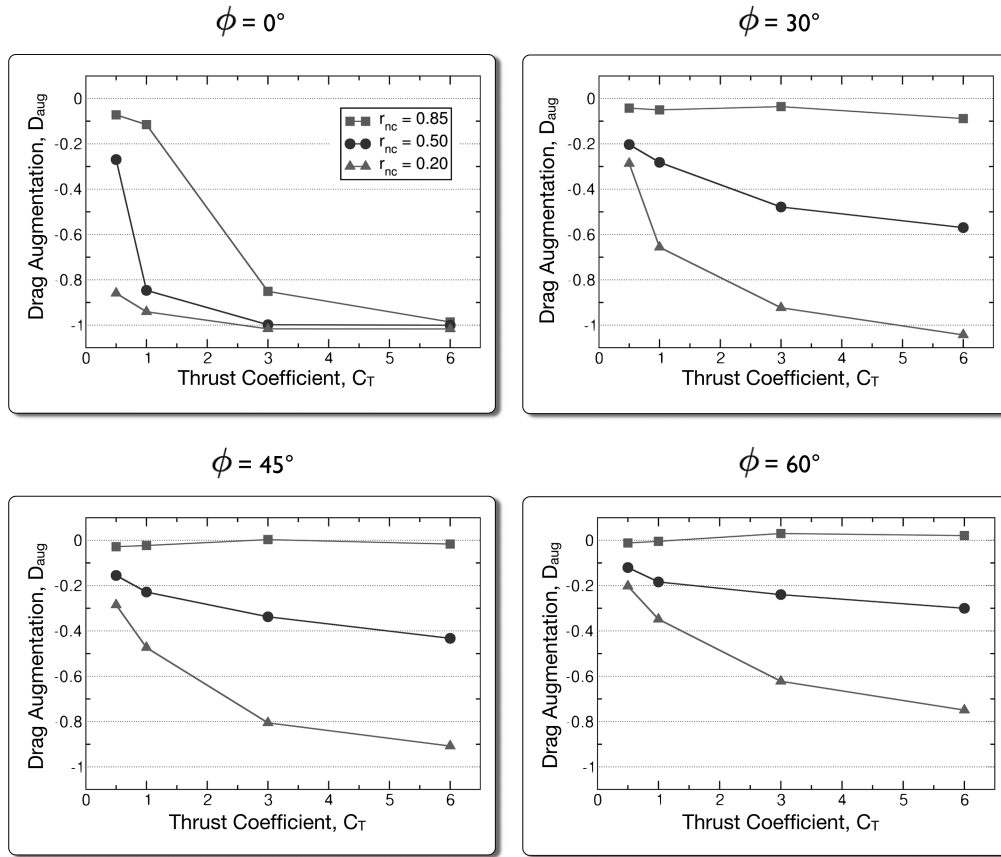
Fig. 14 Drag augmentation values for the baseline tri-nozzle study ($M_\infty = 2$, $\alpha = 0°$).

can experience an increase in pressure (and thus drag) because the maximum surface pressure is determined by the strength of the shock. However, the stagnation pressure loss due to the bow shock severely limits the possibility of drag augmentation. As described in Sec. I, the stagnation pressure loss behind a normal shock at $M_\infty = 2$ is almost 30% and drastically increases at higher M_∞. Previous studies have chosen to focus on these cases despite this, using the engine thrust as a possible means of further deceleration. This brute

force method, however, is based on and limited by the available fuel. The remainder of this study seeks to achieve an alternate means of increasing the deceleration by tapping into this stagnation pressure potential through shock structure manipulation, thus allowing surface overpressures and increased drag. An augmented study is completed next, enlarging the parameter space to include higher Mach numbers and nonzero angles of attack to establish the potential for significant levels of drag augmentation.
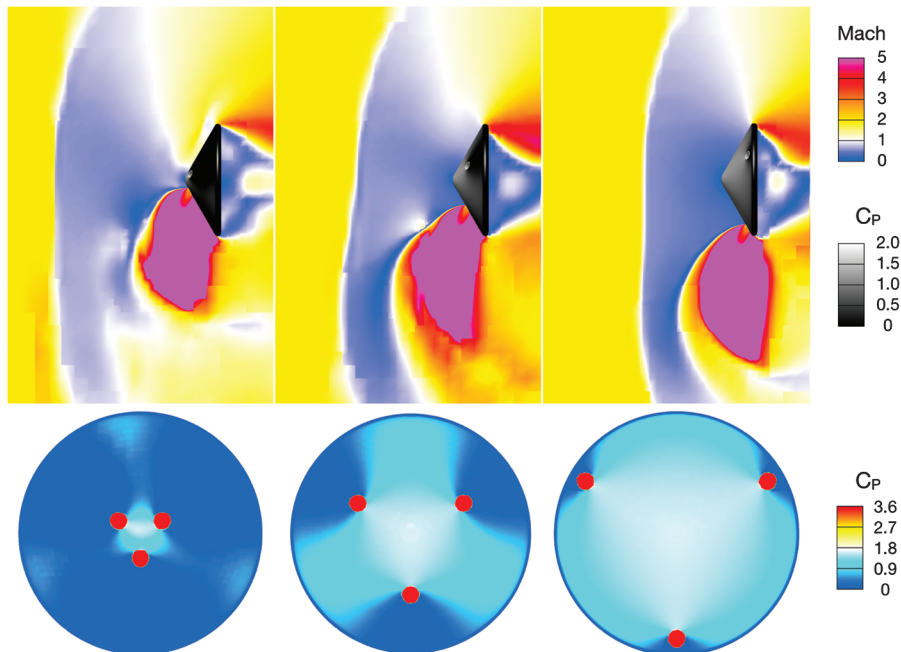

Fig. 15 Flow images showing effect of nozzle location: $\mathcal{P}(M_\infty, \alpha, r_{nc}, \phi, C_T) = \mathcal{P}(2, 0°, \{0.20, 0.50, 0.85\}, 60°, 6)$, from left to right.
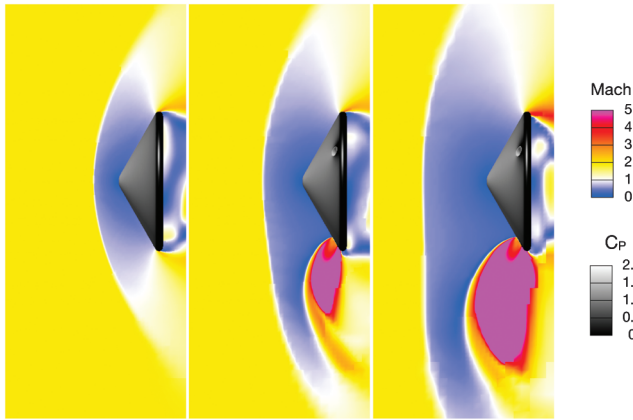
Fig. 16 Visualization of the lengthening of the normal shock portion of the bow shock, causing minimal drag augmentation: $\mathcal{P}(M_\infty, \alpha, r_{nc}, \phi, C_T) = \mathcal{P}(2, 0°, 0.85, 60°, \{0, 1, 3\})$.

Table 3 $C_T = 0$ (jets-off) reference values for the augmented tri-nozzle study: computed C_D over a range of M_∞ and α

α	$M_\infty = 4$	$M_\infty = 6$	$M_\infty = 8$
0°	1.473	1.465	1.465
10°	1.411	1.390	1.379

3. Augmented Tri-Nozzle Study

To investigate trends at higher freestream Mach numbers, the study of Sec. III.B.2 is extended to include $M_\infty = 4, 6, 8$. This study examines cases located along the edges of the hypercube of the parametric space given in Table 2, $\mathcal{P}(M_\infty, \alpha, r_{nc}, \phi, C_T) = \mathcal{P}(\{4, 6, 8\}, \{0°, 10°\}, \{0.20, 0.85\}, \{0°, 60°\}, \{1, 6\})$. In total, 54 cases were run in this study including six jets-off ($C_T = 0$) cases used for reference. Table 3 gives C_D for the six jets-off cases.
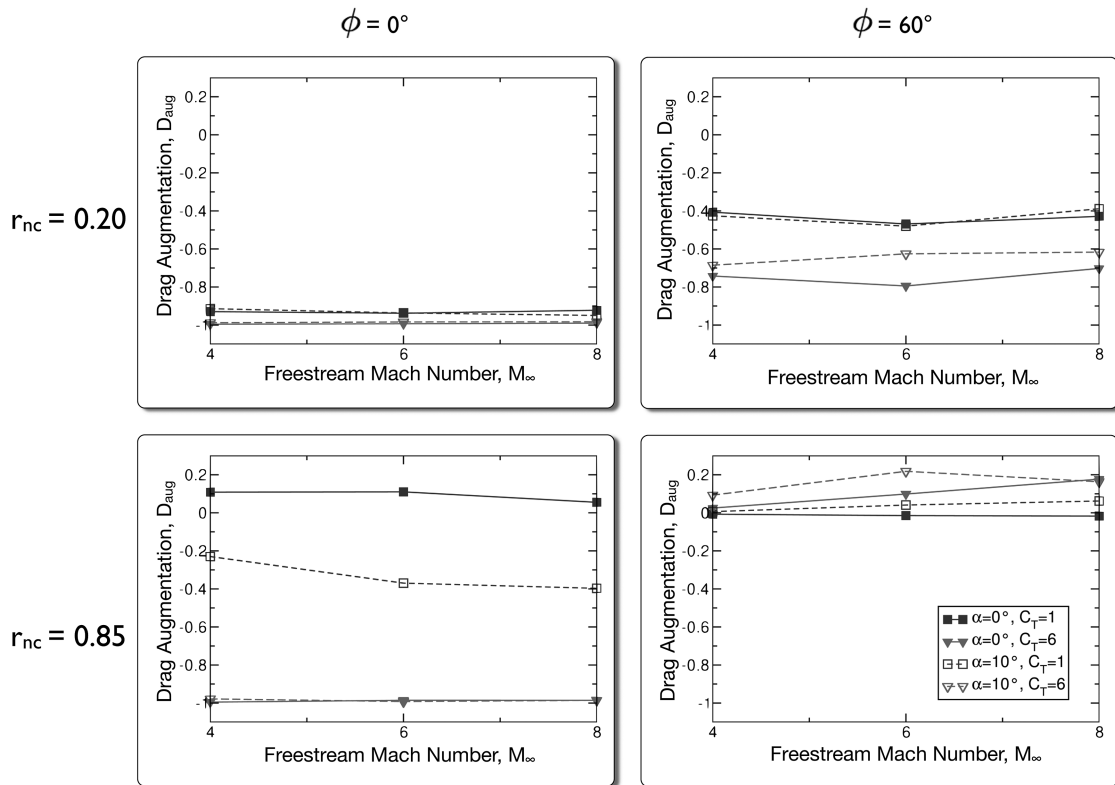

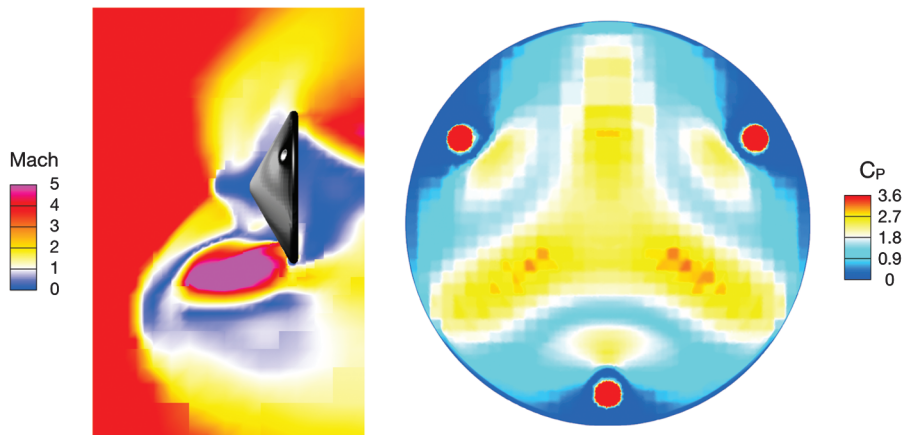**Fig. 17 Drag augmentation values for the augmented tri-nozzle study.**

Fig. 18 Mach contours and capsule face C_P for $\mathcal{P}(M_\infty, \alpha, r_{nc}, \phi, C_T) = \mathcal{P}(4, 0°, 0.85, 0°, 1)$.

Table 4   Values of tested parametric values for
the quad-nozzle study

Variable	Tested values
M_∞	2, 4, 6
α	0°, −5°
r_{nc}	0.5, 0.85
ϕ	0°, 30°
C_T	0, 0.5, 1, 3

Table 5 $C_T = 0$ (jets-off) reference values for the
quad-nozzle study: computed C_D over a range
of M_∞ and α

α	$M_\infty = 2$	$M_\infty = 4$	$M_\infty = 6$
0°	1.523	1.473	1.465
−5°	1.501	1.459	1.446

Drag augmentation values for each case in the study are given in Fig. 17. The D_{ref} used to determine D_{aug} for each run [Eq. (10)] is given by the specific $C_T = 0$ drag value for the corresponding combination of Mach-α. Similar to the previous study, all central nozzle configurations ($r_{nc} = 0.20$) decrease the drag by blocking the capsule face with the plumes, even at higher nozzle tilt angles. However, in this augmented study, several of the peripheral nozzle cases ($r_{nc} = 0.85$) do exhibit substantial drag augmentation (up to 0.218, a 21.8% drag increase).

Figure 18, representing $\mathcal{P}(M_\infty, \alpha, r_{nc}, \phi, C_T) = \mathcal{P}(4, 0°, 0.85, 0°, 1)$ shows the areas of overpressure (yellow and orange) achieved on the capsule face which lead to a drag increase of 10.9%. To aid in visualization of the pertinent flow physics leading to the drag augmentation values achieved in this study, a quad-nozzle study was completed and is described in the next section.

C. Quad-Nozzle Study

The previous tri-nozzle study identified several cases of significant drag augmentation. To further study the physical mechanisms leading to overpressure and drag augmentation, a similar parametric study is completed here using a quad-nozzle model. The additional symmetry provided by the quad-nozzle configuration aids greatly in flowfield visualization. Examples from this study guide a discussion in Sec. III.D of the physical mechanisms responsible for the drag increase.

1. Geometry and Parameterization

The baseline configuration used for this study utilizes similar geometries to those described in the tri-nozzle studies of Sec. III.B. However, we now study a configuration with four equally-spaced nozzles, and A_e/A^* is increased to 20.4 to further expand the jets. The parametric space studied here spans the same five dimensions as the tri-nozzle studies, $\mathcal{P} = \mathcal{P}(M_\infty, \alpha, r_{nc}, \phi, C_T)$, with tested values given in Table 4. In total, 78 cases were run in this study.

2. Results and Analysis

Table 5 gives C_D for the six baseline cases with no SRP which serve as reference values in the drag augmentation calculations [see Eq. (10)]. Drag augmentation values for each case are shown in the plots of Fig. 19, ranging from −1.01 to 0.12.

The most striking observation is that none of the configurations with nozzles at $r_{nc} = 0.50$ produced a total drag augmentation. Even with the decreased jet exit pressures, the plumes in this study remain large enough to produce extensive wakes which result in low pressure and thus low drag on the capsule face. Although several of the $r_{nc} = 0.5$ cases do exhibit areas of overpressure on the capsule face, the extensive wake regions (similar to those in Fig. 15) due to the interior positioning of the plumes counter the overpressures and ultimately result in a decrease in the total drag of the body. Notably, certain cases actually resulted in 100% drag loss due to plume JI, which conveys that SRP, when acting as an aerospike, can seriously decrease the drag seen by an entering body. The remainder of the discussion will focus on the periphery cases ($r_{nc} = 0.85$).
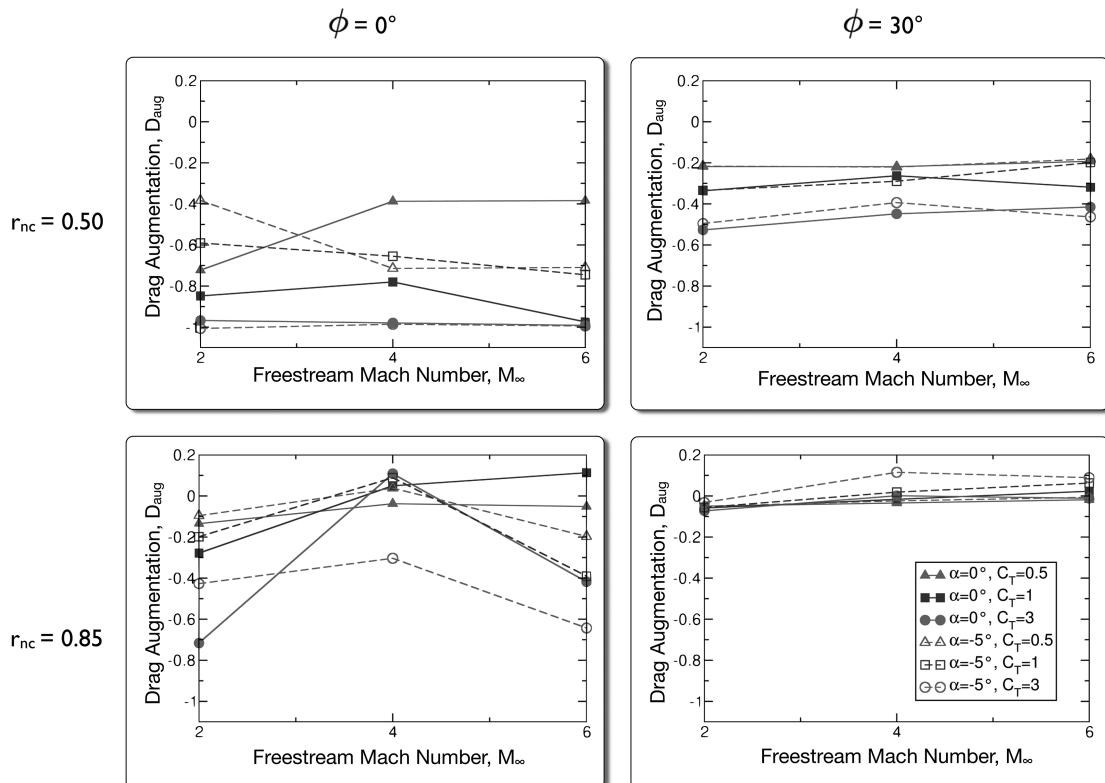
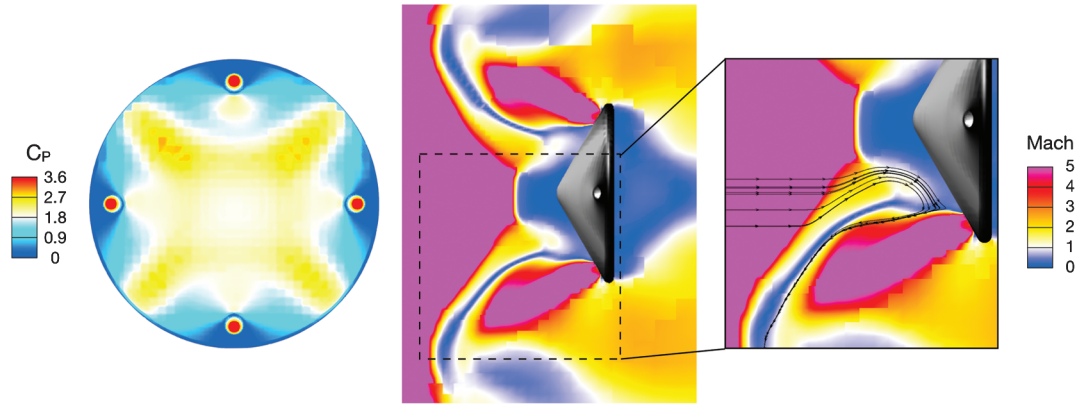Fig. 19   Drag augmentation values for the quad-nozzle study.

Fig. 20 Visualization of capsule face C_P, Mach contours, and a zoomed view showing flow approaching the capsule: $\mathcal{P}(M_\infty, \alpha, r_{\mathrm{nc}}, \phi, C_T) = \mathcal{P}(6, 0°, 0.85, 0°, 1)$.

Examining the effect of variation in Mach number shows that drag augmentation is never achieved in the lowest Mach cases ($M_\infty = 2$) in this study. Extensive flow visualization revealed that the plumes do not penetrate past the capsule bow shock until $M_\infty > 2$, owing to the large shock standoff distance at low Mach numbers. This suggests that the penetration of the jets past the capsule bow shock may play a part in the physics leading to surface overpressures and drag augmentation.

A detailed look at one case, $\mathcal{P}(M_\infty, \alpha, r_{\mathrm{nc}}, \phi, C_T) = \mathcal{P}(6, 0°, 0.85, 0°, 1)$ exhibiting 11.3% drag augmentation (with $C_D = 1.63$), sheds light on the physical mechanisms involved in this drag increase. Figure 20 shows the capsule face overpressures, pitch-plane Mach contours, and a close-up of the flow near the nozzle. The capsule face plot shows C_P with the color map again chosen such that white represents $C_P = C_{P_{ONS}}$ (1.8 for $M_\infty = 6$), overpressures ($C_P > C_{P_{ONS}}$) are yellow and red, and underpressures ($C_p < C_{P_{ONS}}$) are blue. Plume and shock visualizations are shown using a color map chosen as before such that the sonic line is white, supersonic flows are yellow to red, and subsonic flows are blue.

In this figure, we see that as a jet penetrates into the freestream flow, a bow shock system forms around the plume itself, creating a plume-shock. Flow passing through the oblique section of this plume-shock is turned towards the capsule face and decelerated by the oblique shock with a subsequent decrease in stagnation pressure. This P_o decrease, however, is much less extreme than the decrease experienced by flow passing through the capsule bow shock ($P_{oOS} > P_{oNS}$). In this way, flow having passed through the oblique section of the plume-shock is able to reach much higher pressures as it decelerates towards the capsule face, consistent with the overpressures seen in the same figure.

Figure 21 shows stagnation temperature isosurfaces in the shocks and plumes, offering a more three-dimensional understanding of the flow. This figure makes more apparent the oblique shock surfaces, or skirts (gray), wrapping around each jet (orange). These shock skirts, oblique to the flow, allow flow deceleration and compression through oblique rather than normal shocks. With lower shock-losses, this flow recovers higher pressure values when it ultimately impinges upon the capsule face, yielding high-pressure areas on the surface behind each shock skirt. Predictably, the very center of the capsule face lying behind a normal shock at M_∞ is white. The highest values of overpressure ($C_{p,\max} = 2.97$ on the capsule face), seen as the yellow X-shaped pattern on the capsule face, occur between adjacent oblique shock skirts, implying that oblique shock–shock interactions have a role in the drag augmentation achieved in this case. These observations led to the development of a flow model for drag augmentation, described in more detail in Sec. III.D. At 2.97, the
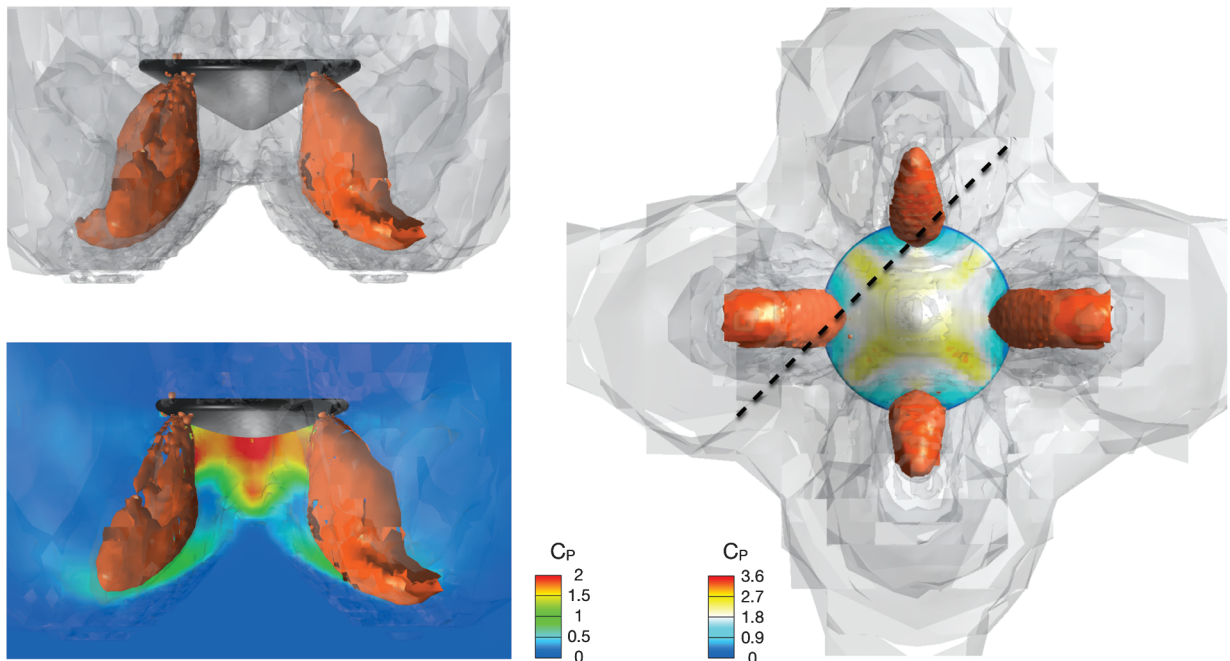

Fig. 21   Three-dimensional representation of the plume-shocks, C_P on a diagonal cutting-plane intersecting two adjacent nozzles, and an axial view showing surface C_P.
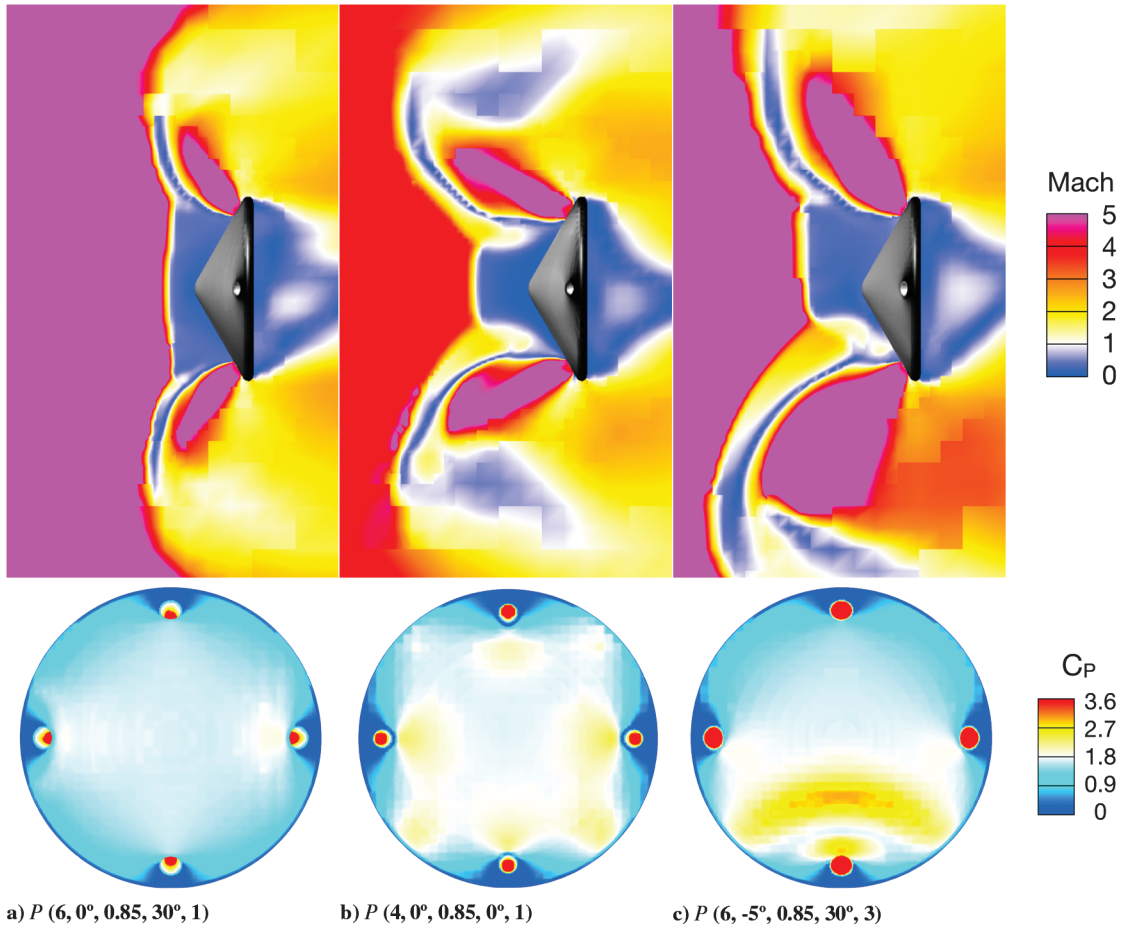
a) P (6, 0°, 0.85, 30°, 1)   b) P (4, 0°, 0.85, 0°, 1)   c) P (6, -5°, 0.85, 30°, 3)

Fig. 22   Various flows leading to drag augmentation in the quad-nozzle study. $\mathcal{P} = \mathcal{P}(M_\infty, \alpha, r_{nc}, \phi, C_T)$.

maximum overpressures on the capsule face are fully 60% higher than $C_{P_{oNS}}$ for this case which is only 1.82.

Further examination of the 11 cases experiencing drag augmentation in this study indicated three different overpressure patterns, shown in Fig. 22. As described previously in Sec. III.B.2, a minimal amount of drag augmentation (2.3% in this case) can be achieved through flattening of the bow shock across the capsule face (Fig. 22a). Figure 22b displays the same oblique shock mechanism described in detail above, here with a drag augmentation of 4.9%. Figure 22c shows a typical case at $\alpha = -5°$ which achieved 8.9% from the large overpressure occurring around a single nozzle due to the oblique shock skirt around the lower jet.

Analysis of $\mathcal{P}$-variable trends reinforces the proposed D_{aug} mechanism. As previously noted, low M_∞ cases do not see penetration of the plumes past the capsule bow shock, thus preventing the formation of the plume-shock skirt. As expected, no drag augmentation is seen in these cases. Similarly, nozzles at high tilt angles (high ϕ) must be coupled with strong jets (high C_T) to allow jet penetration past the capsule bow shock to trigger the D_{aug} mechanism. In addition, configurations with large nozzle tilt angles see less D_{aug} at $\alpha = 0°$ because the flow passing through the oblique shocks is projected onto the jet itself instead of the capsule face. However, holding the capsule at an angle of attack is shown to yield overpressures around a single nozzle even at high values of ϕ.
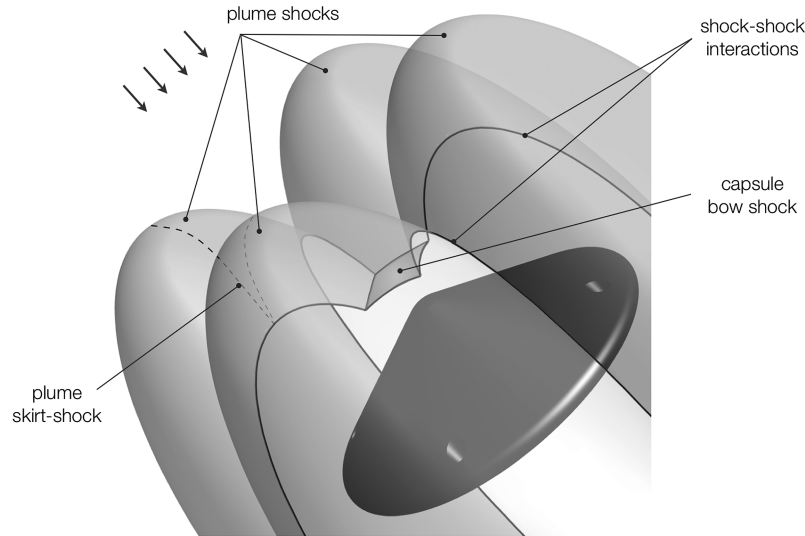
D.   Flow Model for Drag Augmentation

The preliminary parameter studies described in Secs. III.B and III.C indicate the potential for significant drag augmentation through SRP. We now examine the underlying physical mechanisms responsible for the overpressures established on the capsule face, highlighting the capability of this approach to produce meaningful drag augmentation in SRP systems.

Supersonic plumes behave in a manner similar to hard geometry. As the plume penetrates the supersonic freestream, a bow shock system forms, wrapping around the jet plume as seen in Fig. 23a. The skirt of this plume-shock is oblique to the oncoming flow, and freestream flow passing through the oblique section is compressed without experiencing the massive stagnation pressure losses of a normal shock ($P_{oOS} > P_{oNS}$).

In this way, portions of the capsule face surface can be protected from stagnation pressure losses by the oblique shock skirts of the plume-shocks. Moreover, interaction regions between adjacent plume-shock skirts lead to oblique shock–shock interactions (Fig. 23b), further decelerating the oncoming flow and raising the pressure incrementally through multiple oblique shock compressions. This incremental flow deceleration technique allows preservation of stagnation pressure, enabling higher surface pressures and, ultimately, significant drag augmentation.

It is also noteworthy that this curtailment of stagnation pressure losses scales favorably with M_∞, implying that the drag benefits will increase with Mach number. Figure 24 gives P_{o2}/P_{o1} values for both normal and oblique (weak with 20° turning angle) shocks as a function of M_∞, and more importantly shows the increase in the ratio (oblique to normal) of postshock stagnation pressures with increasing Mach number. For example, at $M_\infty = 3$ and $\gamma = 1.4$, the stagnation pressure loss behind a normal shock is about 70% ($P_{oNS}/P_{o1} = 0.328$) while that behind a weak oblique shock with a 20° turning angle is only 20% ($P_{oOS}/P_{o1} = 0.796$). Therefore, at this low Mach number, flow behind an oblique shock stagnates at a pressure 2 times greater than that behind a bow shock. Moreover, increasing M_∞ to 6, at which $P_{oNS}/P_{o1} = 0.030$, allows a post-oblique shock stagnation pressure of almost 13 times greater than P_{oNS}. At Mach 10, the ratio increases to 34, clearly illustrating this favorable Mach scaling. From a trajectory standpoint, more drag at higher Mach numbers translates into increased time for vehicle deceleration.
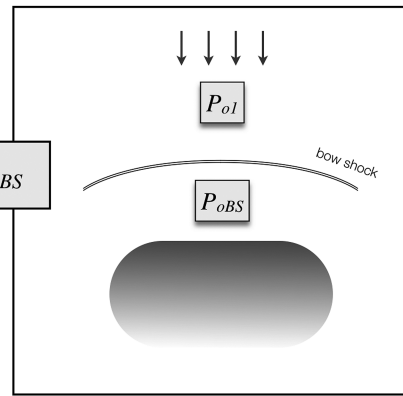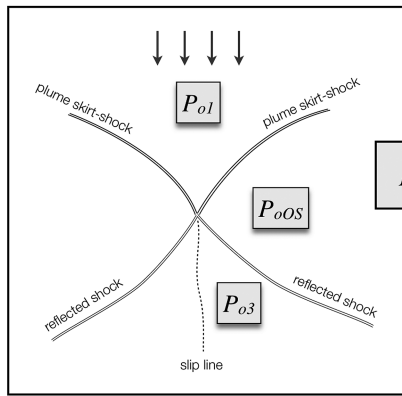
Fig. 23 Flow model for drag augmentation: a) diagram showing plume-shocks resulting from retroplumes (not pictured), where solid lines indicate shock–shock interactions (including oblique interactions between adjacent plume-shock skirts), b) two-dimensional diagram representing a slice through adjacent plume-shock skirts showing the interaction between two plume skirt-shocks, which are indicated by dotted lines in (a), and c) stagnation pressure behind a bow shock P_{oBS} (similar to P_{oNS}).
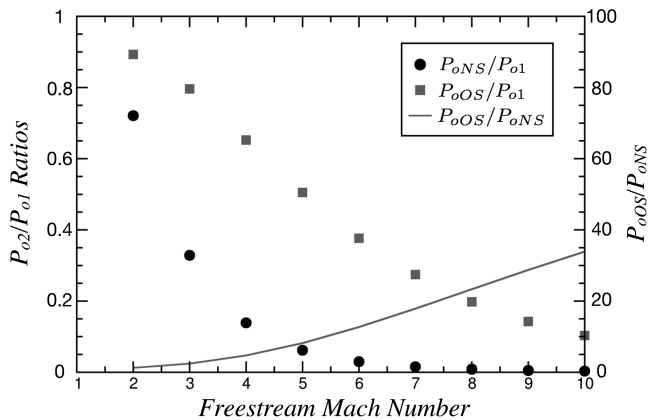
Fig. 24 Stagnation pressure losses for normal (P_{oNS}/P_{o1}) and oblique shocks (P_{oOS}/P_{o1}), for $\gamma = 1.4$. P_{oOS}/P_{oNS} also plotted as a function of M_∞.

IV. Conclusions

Current Mars missions are already challenging the mass limits of existing EDL technology. With heavier payloads on the horizon, future missions must undertake the development of new deceleration systems. This work used large-scale numerical parametric studies to examine the aerodynamic performance of a broad spectrum of SRP systems and to identify key physical mechanisms that may be exploited for deceleration.

Three parametric studies were performed on tri- and quad-nozzle configurations, encompassing over 181 cases. These studies spanned a Mach range from 2 to 8 and considered a range of thrust coefficients with retrojet nozzles located both near the center of the capsule face and towards the periphery at tilt angles from 0° to 60°. Drag data was presented for thrust coefficients ranging from 0 to 6. Drag augmentation values on the order of 20% were observed, resulting from local surface pressures 60% higher than that achieved behind a normal shock. Conversely, the results in much of the previous SRP literature were confirmed by many of the parametric cases exhibiting a staggering decrease in drag (up to 104%), demonstrating that when applied incorrectly, retrojets have the capacity to act as aerospikes.

In addition, this work identified two mechanisms for SRP drag augmentation. Even without jet penetration, straightening of the bow shock can produce a minor increase in drag, with maximum pressure behind the lengthened normal section limited to stagnation pressure behind a normal shock. A more significant drag augmentation mechanism is based on shock manipulation, in which the retrojets serve as oblique shock generators. With the plume-shock skirts protecting the capsule from massive normal shock stagnation pressure losses, the flow approaching the capsule face is compressed by multiple oblique shocks, enabling significant overpressure on the capsule face.

This physical model of SRP drag augmentation is fully consistent with data from the parametric studies. By increasing the influence of the shock skirts and creating more oblique-oblique interaction events, the stagnation pressure losses can be kept to a minimum while still establishing significant overpressures on the surface. In addition, minimizing the plume wake through control of jet size or placement allows for even greater drag values. This approach of oblique shock over normal shock compression also offers the potential for elevated drag augmentation with increasing Mach number, allowing earlier deceleration of the entry system. Moreover, wielding SRP at higher altitudes would alleviate the need for stronger (more expensive) jets.

Since the proposed mechanism for improving deceleration is grounded in altering the capsule drag rather than increasing the jet thrust, retrojet fuel mass becomes less of an issue. With a fundamental physical mechanism for drag augmentation identified, follow-on studies are planned to exploit this alternative approach to SRP implementation. Future work will include a comparison of this steady, inviscid modeling approach to more relevant experimental data from upcoming wind tunnel experiments. In addition, an optimization study and associated entry trajectory analysis will be completed in order to fully quantify the potential payoff in terms of delivered mass and establish the feasibility of SRP as a high-mass deceleration technique for future Mars EDL challenges.

Acknowledgments

References

[1] Braun, R. D., and Manning, R. M., "Mars Exploration Entry, Descent, and Landing Challenges," *Journal of Spacecraft and Rockets*, Vol. 44, No. 2, March–April 2007, pp. 310–323.
doi:10.2514/1.25116

[2] Drake, B. G., ed., *Human Exploration of Mars Design Reference Architecture 5.0*, NASA Rept. SP-2009-566, July 2009.

[3] Korzun, A. M., Cruz, J. R., and Braun, R. D., "A Survey of Supersonic Retropropulsion Technology for Mars Entry, Descent, and Landing," *Journal of Spacecraft and Rockets*, Vol. 46, No. 5, Sept.–Oct. 2009, pp. 929–937.
doi:10.2514/1.41161

[4] Love, E. S., and Grigsby, C. E., "Some Studies of Axisymmetric Free Jets Exhausting from Sonic and Supersonic Nozzles into Still Air and into Supersonic Streams," NACA Research Memorandum NACA-RM-L54L31, NASA Langley Aeronautical Lab., Langley Field, VA, May 1955.

[5] Stalder, J. R., and Inouye, M., "A Method of Reducing Heat Transfer to Blunt Bodies by Air Injection," NACA Research Memorandum NACA-RM-A56B27a, NASA Ames Aeronautical Lab., Moffett Field, CA, May 1956.

[6] Romeo, D. J., and Sterrett, J. R., "Flow Field for Sonic Jet Exhausting Counter to a Hypersonic Mainstream," *AIAA Journal*, Vol. 3, No. 3, March 1965, pp. 544–546.
doi:10.2514/3.2907

[7] Finley, P. J., "The Flow of a Jet from a Body Opposing a Supersonic Free Stream," *Journal of Fluid Mechanics*, Vol. 26, No. 2, 1966, pp. 337–368.
doi:10.1017/S0022112066001277

[8] McGhee, R. J., "Effects of a Retronozzle Located at the Apex of a 140 Deg Blunt Cone at Mach Numbers of 3.00, 4.50, and 6.00," NASA TN-D-6002, NASA Langley Research Center, Hampton, VA, Jan. 1971.

[9] Meyer, B., Nelson, H. F., and Riggins, D. W., "Hypersonic Drag and Heat-Transfer Reduction Using a Forward-Facing Jet," *Journal of Aircraft*, Vol. 38, No. 4, July–Aug. 2001, pp. 680–686.
doi:10.2514/2.2819

[10] Hatashi, K., Aso, S., and Tani, Y., "Numerical Study of Thermal Protection System by Opposing Jet," 43rd AIAA Aerospace Sciences Meeting, AIAA Paper 2005-188, Reno, NV, Jan. 2005.

[11] Chang, C.-L., Venkatachari, B. S., and Cheng, G. C., "Effect of Counterflow Jet on a Supersonic Reentry Capsule," 42nd AIAA/ASME/SAE/ASEE Joint Propulsion Conference, AIAA Paper 2006-4776, Sacramento, CA, July 2006.

[12] Daso, E. O., Pritchett, V. E., Wang, T.-S., Ota, D. K., Blankson, I. M., and Auslender, A. H., "The Dynamics of Shock Dispersion and Interactions in Supersonic Freestreams with Counterflowing Jets," 45th AIAA Aerospace Sciences Meeting, AIAA Paper 2007-1423, Reno, NV, Jan. 2007.

[13] Shang, J. S., "Plasma Injection for Hypersonic Blunt-Body Drag Reduction," *AIAA Journal*, Vol. 40, No. 6, June 2002, pp. 1178–1186.
doi:10.2514/2.1769

[14] Menezes, V., Saravanan, S., Jagadeesh, G., and Reddy, K. P. J., "Experimental Investigations of Hypersonic Flow over Highly Blunted Cones with Aerospikes," *AIAA Journal*, Vol. 41, No. 10, Oct. 2003, pp. 1955–1966.
doi:10.2514/2.1885

[15] Jarvinen, P. O., and Adams, R. H., "The Aerodynamic Characteristics of Large Angled Cones with Retrorockets," NASA Contract No. NAS7-576, Cambridge, MA, Feb. 1970.

[16] Jarvinen, P. O., and Adams, R. H., "The Effects of Retrorockets on the Aerodynamic Characteristics of Conical Aeroshell Planetary Entry Vehicles," AIAA Eighth Aerospace Sciences Meeting, AIAA Paper 70-219, New York, Jan. 1970.

[17] Keyes, J. W., and Hefner, J. N., "Effect of Forward-Facing Jets on Aerodynamic Characteristics of Blunt Configurations at Mach 6," *Journal of Spacecraft and Rockets*, Vol. 4, No. 4, April 1967, pp. 533–534.
doi:10.2514/3.28900

[18] Peterson, V. L., and McKenzie, R. L., "Effects of Simulated Retrorockets on the Aerodynamic Characteristics of a Body of Revolution at Mach Numbers from 0.25 to 1.90," NASA TN D-1300, NASA Ames Research Center, Moffett Field, CA, May 1962.

[19] Aftosmis, M. J., Berger, M. J., and Melton, J. E., "Robust and Efficient Cartesian Mesh Generation for Component-Based Geometry," *AIAA Journal*, Vol. 36, No. 6, 1998, pp. 952–960.
doi:10.2514/2.464

[20] Aftosmis, M. J., Berger, M. J., and Adomavicius, G., "A Parallel Multilevel Method for Adaptively Refined Cartesian Grids with Embedded Boundaries," 38th AIAA Aerospace Sciences Meeting, AIAA Paper 2000-0808, Reno, NV, Jan. 2000.

[21] Nemec, M., and Aftosmis, M. J., "Adjoint Error Estimation and Adaptive Refinement for Embedded-Boundary Cartesian Meshes," 18th AIAA Computational Fluid Dynamics Conference, AIAA Paper 2007-4187, Miami, FL, June 2007.

[22] Nemec, M., and Aftosmis, M. J., "Adjoint Sensitivity Computations for an Embedded-Boundary Cartesian Mesh Method," *Journal of Computational Physics*, Vol. 227, 2008, pp. 2724–2742.
doi:10.1016/j.jcp.2007.11.018

[23] Nemec, M., Aftosmis, M. J., and Wintzer, M., "Adjoint-Based Adaptive Mesh Refinement for Complex Geometries," 46th AIAA Aerospace Sciences Meeting, AIAA Paper 2008-0725, Reno, NV, Jan. 2008.

[24] Venditti, D. A., and Darmofal, D. L., "Grid Adaptation for Functional Outputs: Application to Two-Dimensional Inviscid Flows," *Journal of Computational Physics*, Vol. 176, 2002, pp. 40–69.
doi:10.1006/jcph.2001.6967

[25] Aftosmis, M. J., Berger, M. J., and Murman, S. M., "Applications of Space-Filling Curves to Cartesian Methods for CFD," 42nd AIAA Aerospace Sciences Meeting, AIAA Paper 2004-1232, Reno, NV, Jan. 2004.

[26] Berger, M. J., Aftosmis, M. J., and Murman, S. M., "Analysis of Slope Limiters on Irregular Grids," 43rd AIAA Aerospace Sciences Meeting, AIAA Paper 2005-0490, Reno, NV, Jan. 2005.

[27] Berger, M. J., Aftosmis, M. J., Marshall, D. D., and Murman, S. M., "Performance of a New CFD Flow Solver Using a Hybrid Programming Paradigm," *Journal of Parallel and Distributed Computing*, Vol. 65, No. 4, 2005, pp. 414–423.
doi:10.1016/j.jpdc.2004.11.010

[28] Aftosmis, M. J., and Rogers, S. E., "Effects of Jet-Interaction on Pitch Control of a Launch Abort Vehicle," 46th AIAA Aerospace Sciences Meeting, AIAA Paper 2008-1281, Reno, NV, Jan. 2008.

[29] Aftosmis, M. J., and Nemec, M., "Exploring Discretization Error in Simulation-Based Aerodynamic Databases," *Proceedings of the 21st International Conference on Parallel Computational Fluid Dynamics*, edited by R. Biswas, DEStech Publications, Lancaster, PA, May 2009.

[30] Murman, S. M., Aftosmis, M. J., and Nemec, M., "Automated Parameter Studies Using a Cartesian Method," NASA TR NAS-04-015, NASA Ames Research Center, Moffett Field, CA, Nov. 2004.

[31] Wintzer, M., Nemec, M., and Aftosmis, M. J., "Adjoint-Based Adaptive Mesh Refinement for Sonic Boom Prediction," 26th AIAA Applied Aerodynamics Conference, AIAA Paper 2008-6593, Honolulu, HI, Aug. 2008.

[32] Nemec, M., and Aftosmis, M. J., "Computations of Aerodynamic Performance Databases Using Output-Based Refinement," Invited Lecture, 47th AIAA Aerospace Sciences Meeting, Orlando, FL, Jan. 2009.

[33] Murman, S. M., Aftosmis, M. J., and Berger, M. J., "Numerical Simulation of Rolling-Airframes Using a Multi-Level Cartesian Method," 20th AIAA Applied Aerodynamics Conference, AIAA Paper 2002-2798, St. Louis, MO, June 2002.

[34] Korzun, A. M., and Braun, R. D., "Performance Characterization of Supersonic Retropropulsion for Application to High-Mass Mars Entry, Descent, and Landing," AIAA Atmospheric Flight Mechanics Conference, AIAA Paper 2009-5613, Chicago, IL, Aug. 2009.

[35] Steinfeldt, B. A., Theisinger, J. E., Korzun, A. M., Clark, I. G., Grant, M. J., and Braun, R. D., "High Mass Mars Entry, Descent, and Landing Architecture Assessment," AIAA SPACE 2009 Conference and Exposition, AIAA Paper 2009-6684, Pasadena, CA, Sept. 2009.